1 Supplementary material

The figures and tables included in this section are intended to be shown at conferences.

Table 1: Observed limits on $\mathcal{B}(\tau^- \to \mu^-\mu^+\mu^-)$ for BSM operators with different chirality structures, as described in JHEP 0710 (2007) 039.

BSM operator	$\tau^- \to \mu^-\mu^+\mu^-$ limit at 90% CL ($\times 10^{-8}$)
$\mathrm{d}^2\Gamma_{\mathrm{V}}^{(\mathrm{LL})(\mathrm{LL})}$	4.2
$\mathrm{d}^2\Gamma_{\mathrm{V}}^{(\mathrm{LL})(\mathrm{RR})}$	4.1
$\mathrm{d}^2\Gamma_{\mathrm{rad}}^{(\mathrm{LR})}$	6.8
$\mathrm{d}^2\Gamma_{\mathrm{mix}}^{(\mathrm{LL})(\mathrm{LL})}$	4.4
$\mathrm{d}^2\Gamma_{\mathrm{mix}}^{(\mathrm{LL})(\mathrm{RR})}$	4.6

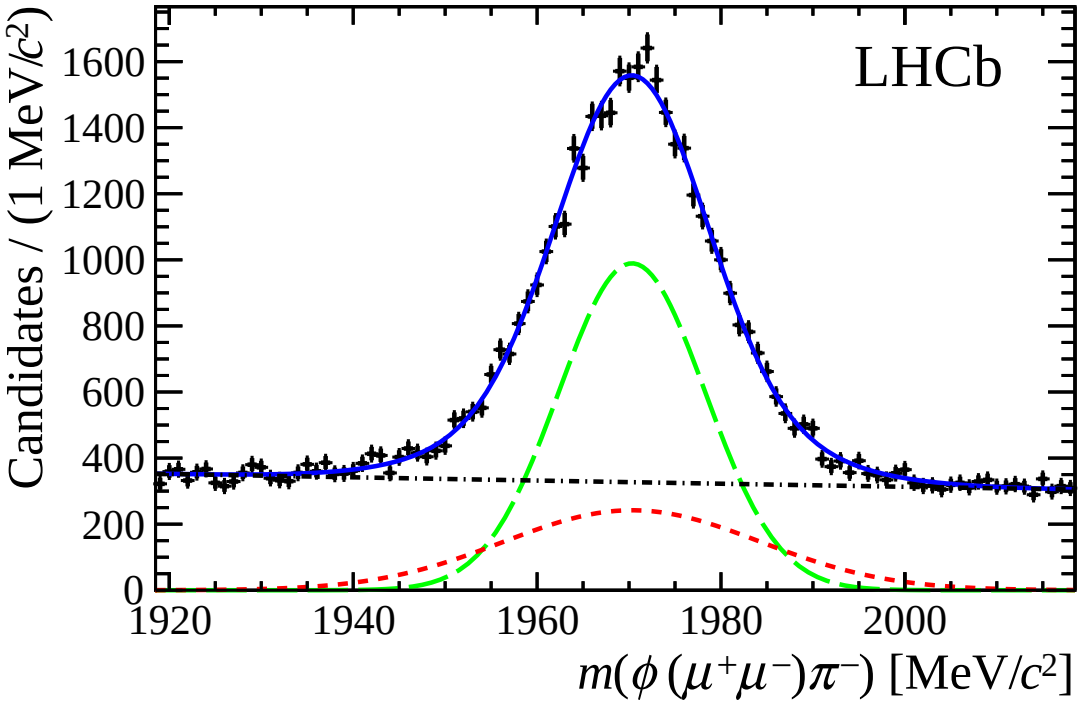

Figure 1: Invariant mass distribution of $\phi(\mu^+\mu^-)\pi^-$ candidates in 7 TeV data. The solid (blue) line shows the overall fit, the long-dashed (green) and short-dashed (red) lines show the two Gaussian components of the D_s^- signal and the dot-dashed (black) line shows the combinatorial background contribution.

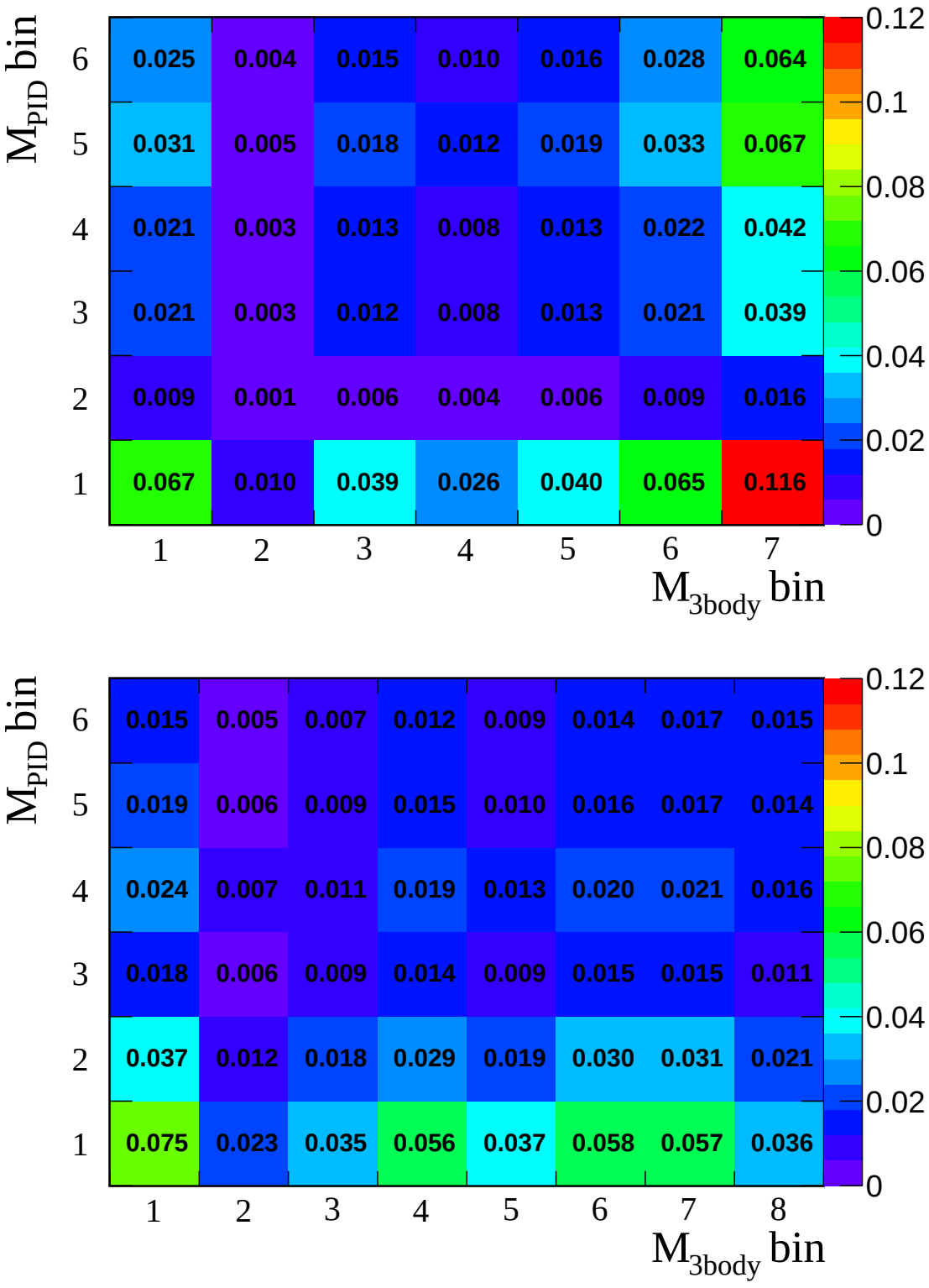

Figure 2: Distributions of simulated signal events in the bins of $\mathcal{M}_{\text{3body}}$ and $\mathcal{M}_{\text{PID}}$ classifier response used in the (top) 7 TeV and (bottom) 8 TeV analyses. The colour scale indicates the fractional contribution in each bin.

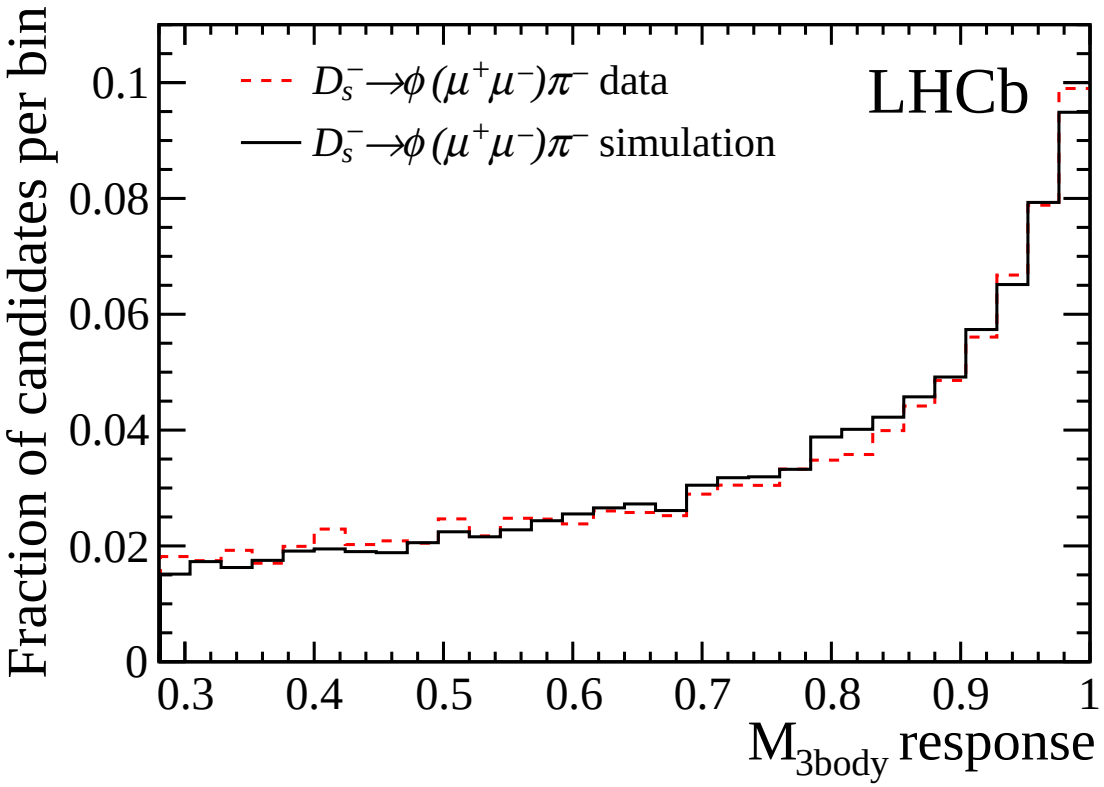

Figure 3: Response of the $\mathcal{M}_{3\text{body}}$ classifier for $D_s^- \to \phi(\mu^+\mu^-)\pi^-$ candidates in data and simulation, in the 8 TeV analysis.

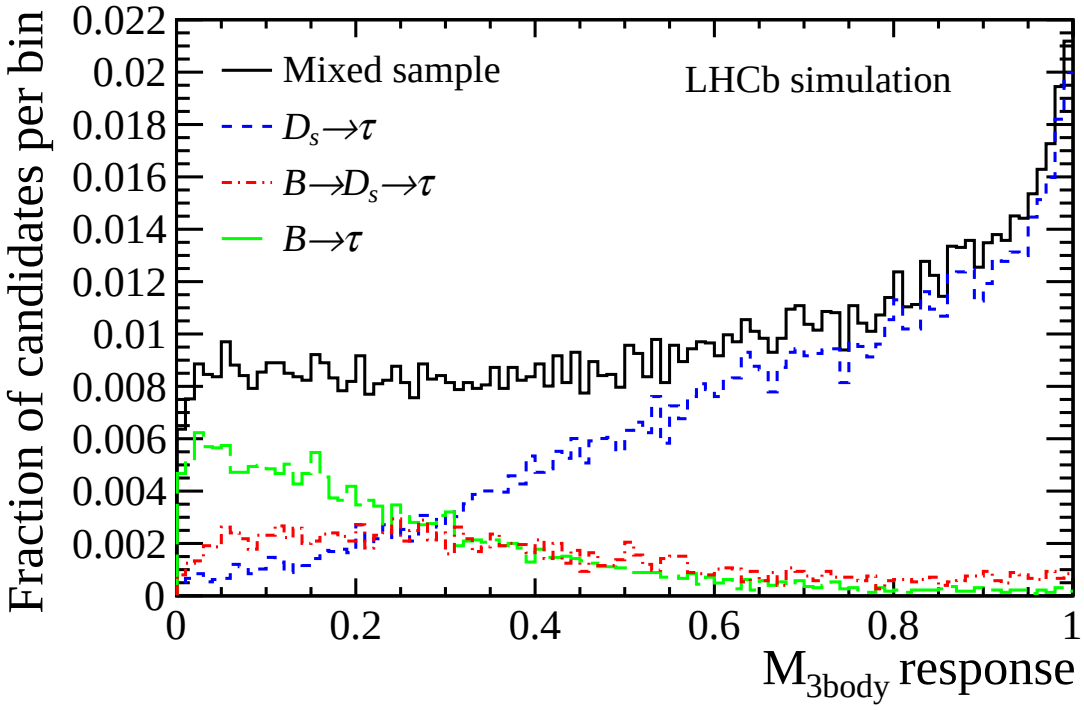

Figure 4: Response of the $\mathcal{M}_{3\text{body}}$ classifier for the mixed sample and different categories of simulated signal events at 8 TeV. The contributions from prompt and secondary D^- decays are negligible and are omitted for clarity.

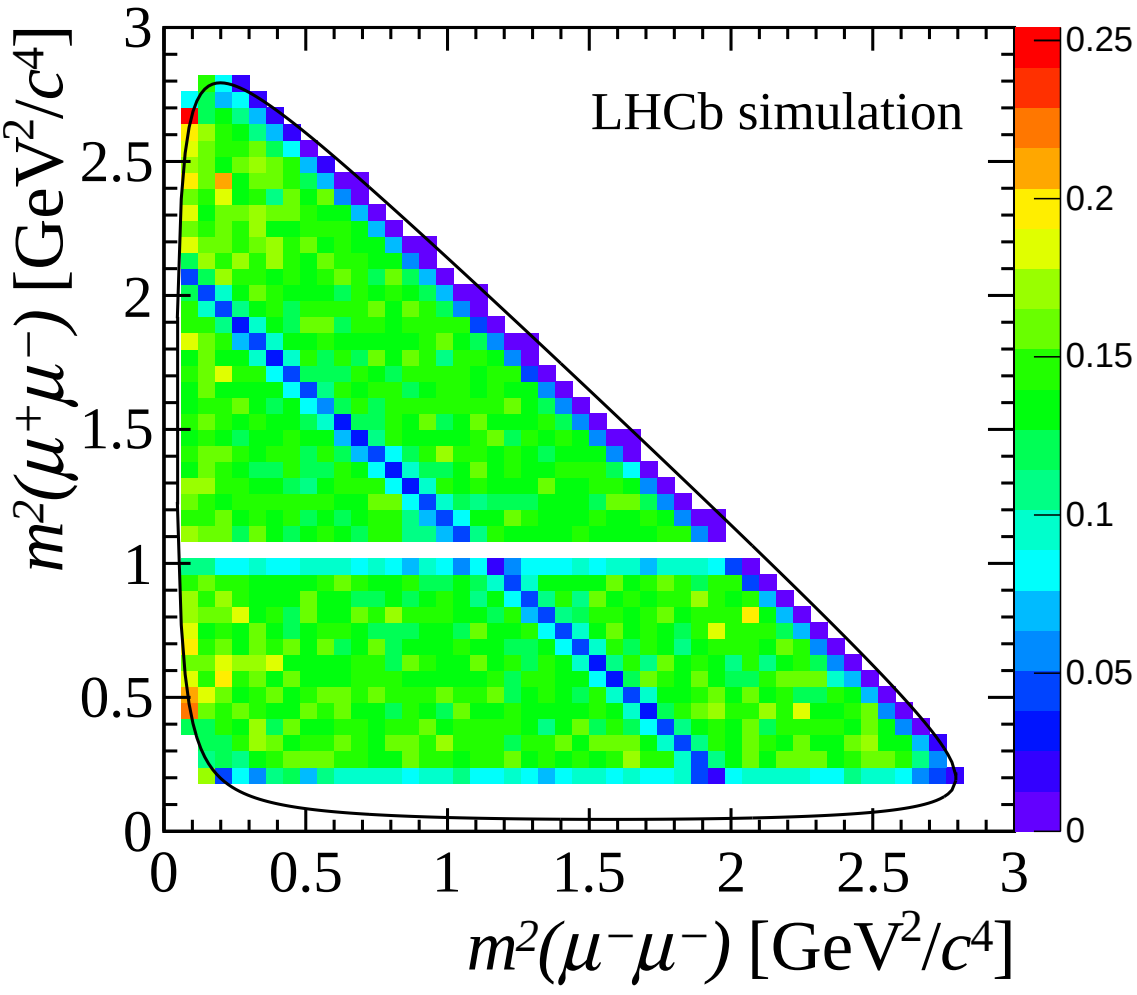

Figure 5: Efficiency of the $\tau^- \to \mu^-\mu^+\mu^-$ selection and trigger requirements for the simulated signal sample as a function of dimuon mass at 8 TeV. The black line indicates the allowed phase-space for the decay. The horizontal white bands indicate the regions of phase-space removed by the $\phi(1020)$ and $D_s^- \to \eta\,(\mu^+\mu^-\gamma)\,\mu^-\bar{\nu}_\mu$ vetoes. The diagonal blue band is also caused by the $\phi(1020)$ veto. The colour scale indicates the fractional contribution in each bin.

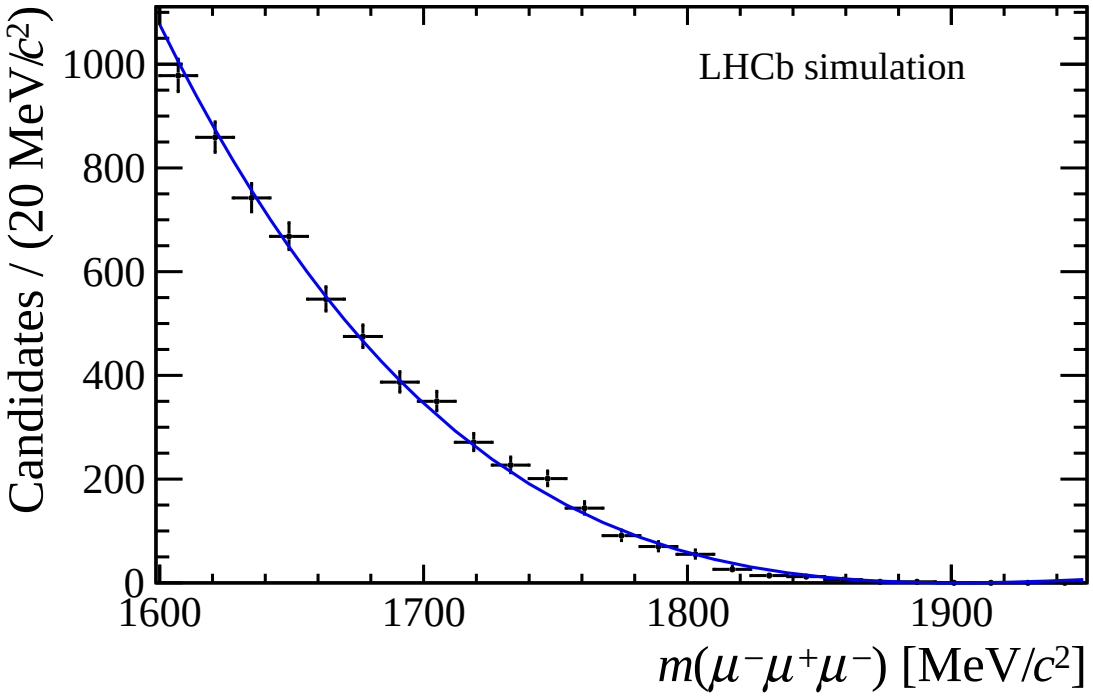

Figure 6: Three-muon invariant mass distribution for simulated $D_s^- \to \eta\,(\mu^+\mu^-\gamma)\,\mu^-\bar{\nu}_\mu$ events at 8 TeV, before the eta veto is applied. The blue line indicates a fit with a fifth-order polynomial multiplied by an exponential function.

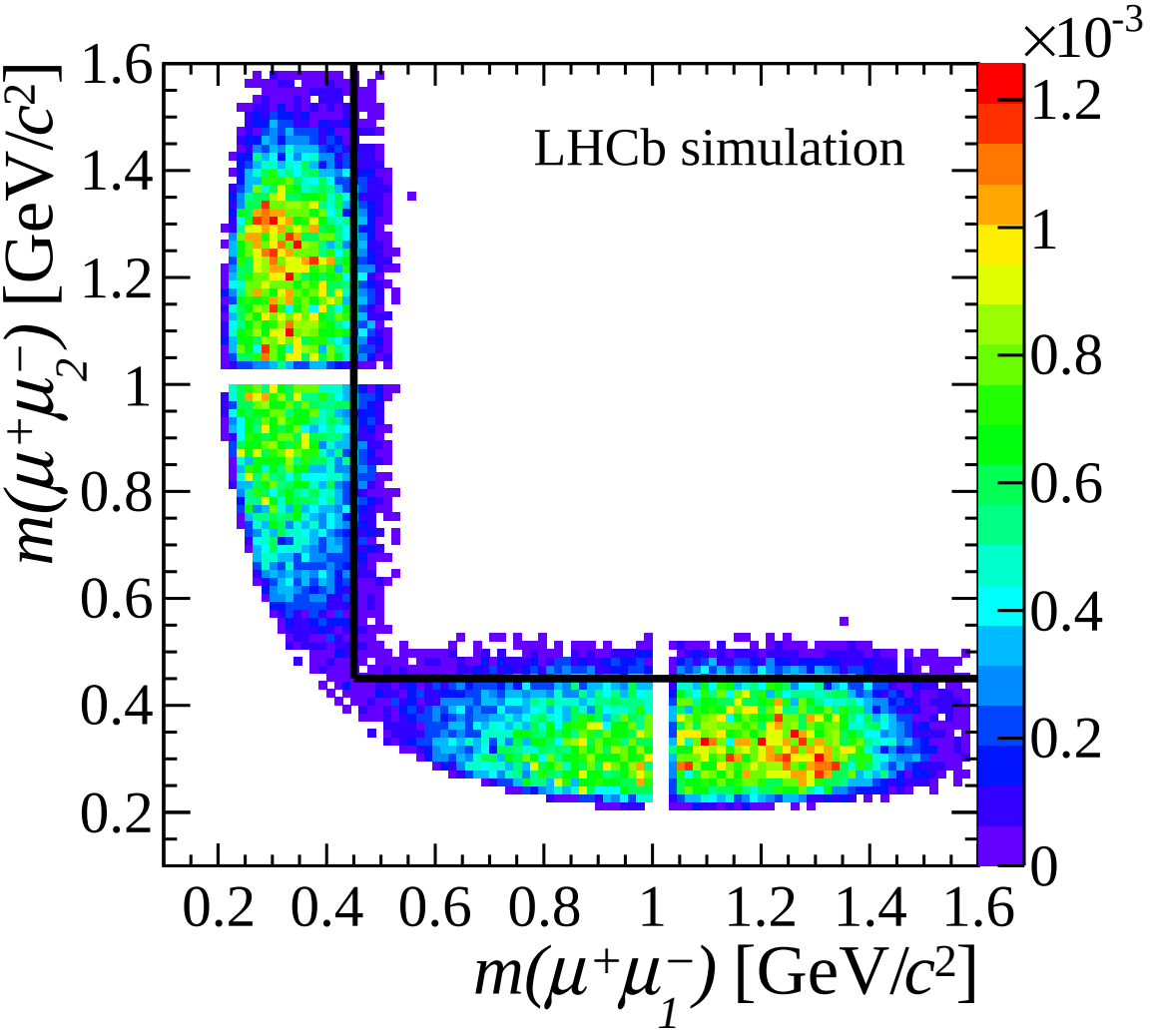

Figure 7: Distribution of simulated $D_s^- \to \eta\,(\mu^+\mu^-\gamma)\,\mu^-\bar{\nu}_\mu$ events as a function of dimuon mass at 8 TeV. This background is removed by excluding the regions to the left of and below the black line. The colour scale indicates the fractional contribution in each bin.

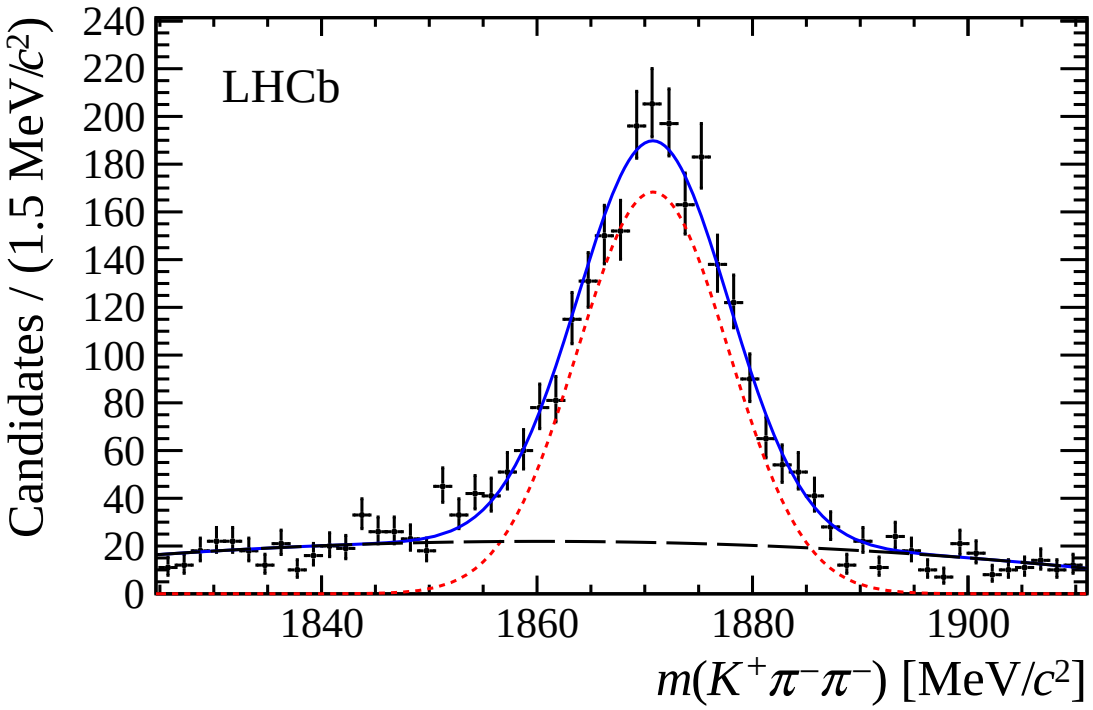

Figure 8: Fit to the data sidebands for the bin $0.61 < \mathcal{M}_{\rm 3body} < 0.70$ and $0 < \mathcal{M}_{\rm PID} < 0.40$ under the $K^+\pi^-\pi^-$ mass hypothesis at 8 TeV. The short-dashed and long-dashed lines indicate the Gaussian and Chebychev polynomial components, respectively. These $\mathcal{M}_{\rm 3body}$ and $\mathcal{M}_{\rm PID}$ bins are not used in the analysis.

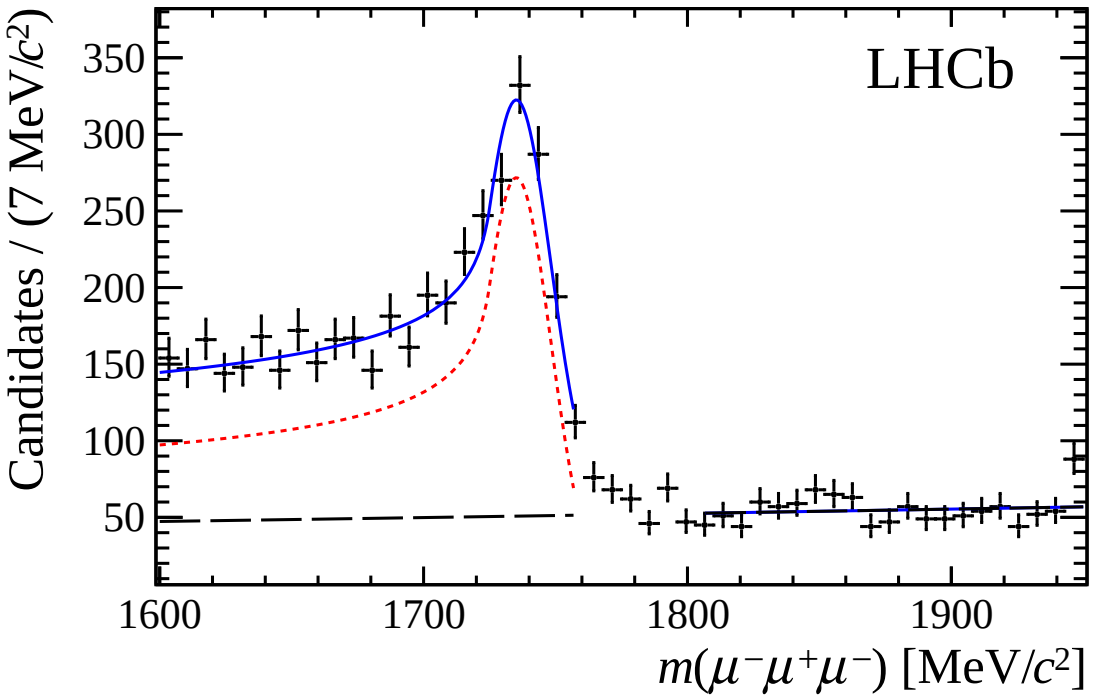

Figure 9: Fit to the data sidebands for the bin $0.61 < \mathcal{M}_{\rm 3body} < 0.70$ and $0 < \mathcal{M}_{\rm PID} < 0.40$ under the $\mu^-\mu^+\mu^-$ mass hypothesis at 8 TeV. The short-dashed line indicates a Crystal Ball function (a Gaussian core with a power-law lower tail) describing the $D^- \to K^+\pi^-\pi^-$ background, the long-dashed line the exponential background and the solid line the total fit function. These $\mathcal{M}_{\rm 3body}$ and $\mathcal{M}_{\rm PID}$ bins are not used in the analysis.